



CHORUS

This is the accepted manuscript made available via CHORUS. The article has been published as:

Finite-temperature properties of antiferroelectric PbZrO_3 from atomistic simulations

B. K. Mani, S. Lisenkov, and I. Ponomareva

Phys. Rev. B **91**, 134112 — Published 27 April 2015

DOI: [10.1103/PhysRevB.91.134112](https://doi.org/10.1103/PhysRevB.91.134112)

Finite-Temperature Properties of Antiferroelectric PbZrO_3 from atomistic simulations

B. K. Mani,¹ S. Lisenkov,¹ and I. Ponomareva¹

¹*Department of Physics, University of South Florida, Tampa, Florida 33620, USA*

Abstract

Antiferroelectrics are under extensive reexamination owing to their unique properties and technological promise. Computationally, they pose a challenge for predictive modeling as they often do not possess well defined localized electric moments and exhibit a delicate energetic balance between polar and antipolar phases. We propose a first-principles-based atomistic model for the prototype antiferroelectric PbZrO_3 that captures accurately a wide range of its properties. Application of the model to study finite-temperature properties of PbZrO_3 under external electric field and hydrostatic pressure aids in achieving a coherent picture of this intriguing material. In particular, our simulations predict: i) the existence of a strong coupling between the antiferrodistortive motion of oxygen octahedra and the antipolar distortion in a wide range of temperatures and electric fields; ii) a linear temperature dependence for the critical field associated with the antiferroelectric to ferroelectric phase transition; and iii) a stabilizing effect of the hydrostatic pressure on the phase transition in PbZrO_3 .

PACS numbers: 77.80.B-,63.70.+h,64.60.Bd

Antiferroelectrics form a class of materials which are characterized by an antipolar crystal structure that has an energetically competitive polar counterpart¹. Due to a variety of attractive functionalities offered by these materials there is an increased interest for their use in the technological applications. Some examples include energy and charge storage devices, electrocaloric refrigerators and high-strain actuators and transducers²⁻⁸. Interestingly, unlike their polar counterparts - ferroelectrics - antiferroelectrics are far less understood. Indeed, even their definition remains debatable for decades. The main difficulty in defining these fascinating materials arise from the fact that unlike their magnetic analogue - antiferromagnets - the majority of antiferroelectric do not have well defined localized electric moments. As a result in defining antiferroelectrics it is essential to add the energy criterion that requires the existence of a ferroelectric phase that is energetically competitive with the antiferroelectric one. The absence of well defined localized moments poses many challenges for developing predictive models of these materials. Indeed, the simple models of reorientable moments localized on two different sublattices are mostly inadequate. One may wish to turn to the soft mode approach that has been remarkably successful in understanding ferroelectrics⁹⁻¹³. In such an approach the soft, or unstable, modes are identified (usually in high-symmetry nonpolar phase) and used to construct the energetic description of the material. This approach is powerful when executed within the framework of first-principles computations¹⁴. At the same time, the drawback is that such computations only provide the zero Kelvin picture.

In case of ferroelectrics the latter difficulty has been eliminated by combining the soft mode approach with classical simulations⁹. The case of antiferroelectrics, however, is more challenging since the unstable mode is not in the center of the Brillouin zone. Moreover, the method should capture the delicate energy competition between the zone-center polar mode and the off-center antipolar mode^{15,16}. These challenges perhaps explain the lack of computational methods capable of providing an atomistic description of antiferroelectrics for practical use and within technologically relevant temperature range.

In this paper we develop such a computational approach that provides an accurate atomistic description of antiferroelectrics at finite temperatures from first principles. We then apply this approach to study one of the most intriguing antiferroelectric, PbZrO_3 . The recently renewed interest in this material^{1,17-21} is driven by its special role as the prototype antiferroelectric and its technological importance. PbZrO_3 exhibits a variety of unique

and practically useful properties such as electric-field induced phase transition from an antiferroelectric (AFE) to a ferroelectric (FE) state, large electrostriction coefficients, giant electrocaloric effects¹. PbZrO_3 has been widely studied both experimentally^{22–28} and computationally^{15,20,21,29–32} with majority of computational studies focused on zero Kelvin properties of this materials. Interestingly, despite its special status as the prototype antiferroelectric our understanding of this material is far from complete. In particular, it remains controversial whether there exists an intermediate, possibly ferroelectric phase, close to the paraelectric to antiferroelectric phase transition^{19,33–38}. The precise origin of antiferroelectricity in this material is being revisited¹⁷. It is currently not well understood how the intrinsic critical fields that induce AFE-FE phase transition depend on the temperature and what is the effect of the hydrostatic pressure on the phase transition. As a result a coherent picture of this material is presently missing. The purpose of this work is to use our first-principles-based approach to provide a comprehensive evaluation of PbZrO_3 properties under applied electric field and hydrostatic pressure in a wide temperature range. In particular, we look into the temperature evolution of PbZrO_3 electric properties, AFE-FE phase transition, critical fields. We study the field and temperature evolution of the leading order parameters as well as the effect that the hydrostatic pressure has on them.

We begin by developing the soft mode based effective Hamiltonian for PbZrO_3 from first-principles. The ground state structure of PbZrO_3 is an antiferroelectric orthorhombic distorted perovskite structure with an associated space group $Pbam$ ^{22–24}. The dominant distortions are from the Σ_2 ($q = \frac{2\pi}{a}(1/4, 1/4, 0)$) and R_4^+ ($q = \frac{2\pi}{a}(1/2, 1/2, 1/2)$) modes. While distortion associated with the Σ_2 mode is responsible for the antipolar arrangements of the lead ions along $[110]$ direction, the R_4^+ distortion arises due to the oxygen octahedra rotation around $[110]$ direction³⁹. We first reproduce the ground state structure of PbZrO_3 in density functional theory (DFT) calculations carried out using the VASP software^{40,41}. For exchange-correlation we employ the local density approximation^{42,43} energy functional together with the projector-augmented wave method^{41,44} to represent the ionic cores. The structural distortions are then analyzed using ISOTROPY software⁴⁵. Fig. 1 gives the amplitudes of different structural distortions along with the cumulative change in energy associated with the addition of each distortion. Note that the energy of undistorted cubic structure is chosen as the zero energy. We find that Σ_2 and R_4^+ are structurally and energetically the most influential distortions. Indeed these two distortions together with the elastic

deformations provide more than 92% of the energy gain associated with the distortion of the ideal cubic perovskite structure. Based on this analysis we build our model to include Σ_2 and R_4^+ modes and strain deformations. Σ_2 and R_4^+ modes are localized on A and B sites of the ABO_3 unit cell, respectively, following the approach of Ref.⁴⁶. Furthermore, the local Σ_2 mode (or just the local mode), \mathbf{u} , is defined from the atomic displacements in Σ_2 mode, while the local R_4^+ mode (or AFD local mode), $\boldsymbol{\omega}$, is defined from $\Delta\mathbf{r} = \frac{a_0}{2}\hat{\mathbf{R}}_{ij} \times (\boldsymbol{\omega}_i - \boldsymbol{\omega}_j)$ ⁴⁶, where $\Delta\mathbf{r}$ is the oxygen displacement in a mode, $\hat{\mathbf{R}}_{ij}$ is the unit vector that connects unit cells i and j , a_0 is the cubic lattice constant. Both \mathbf{u} and $\boldsymbol{\omega}$ are three-dimensional vectors. Thus defined \mathbf{u} has a polar character and is proportional to the local dipole moment in the unit cell, while $\boldsymbol{\omega}$ is nonpolar and describes antiferrodistortive (AFD) oxygen octahedron tilts about the pseudocubic axes. The corresponding order parameters are computed by averaging the local modes in the associated point of the Brillouin zone.

The energy of the structure (the effective Hamiltonian) is expanded in symmetry invariants and written as

$$\begin{aligned}
E^{\text{tot}} = & E^{\text{AFE}}(\{\mathbf{u}_i\}) + E^{\text{AFD}}(\{\boldsymbol{\omega}_i\}) + E^{\text{elas}}(\{\boldsymbol{\eta}_i\}) + E^{\text{AFE-elas}}(\{\mathbf{u}_i, \boldsymbol{\eta}_i\}) \\
& + E^{\text{AFD-elas}}(\{\boldsymbol{\omega}_i, \boldsymbol{\eta}_i\}) + E^{\text{AFE-AFD}}(\{\mathbf{u}_i, \boldsymbol{\omega}_i\}),
\end{aligned} \tag{1}$$

where E^{AFE} is the energy associated with the antiferroelectric Σ_2 mode and includes contributions from the dipole-dipole interactions, short-range interaction, and on-site self energy as defined in Ref.⁴⁷. E^{AFD} gives the energy due to the AFD mode that is similar to E^{AFE} but excludes the dipole-dipole interactions as AFD local modes are nonpolar. The third term, E^{elas} , is the elastic energy associate with the unit cell deformation⁴⁷. The terms $E^{\text{AFE-elas}}$, $E^{\text{AFD-elas}}$, and $E^{\text{AFE-AFD}}$ are the energy contributions due the interactions between the AFE mode and the strain, the AFD mode and the strain, and the AFE and AFD modes, respectively^{46,47}. The parameters that describe the interactions in Eq. (1) are derived from the local density approximation based DFT calculations and are given in Table I. It should be noted that a similar computational approach was previously developed to study $\text{Pb}(\text{Zr}_{1-x}\text{Ti}_x)\text{O}_3$ solid solution near its morphotropic phase boundary and led to a variety of insights and computational predictions⁴⁸. The main difference between the approach proposed here and the one developed in Ref.48 is the parametrization. Our parametrization targets pure PbZrO_3 , while the parametrization of Ref.48 focuses on $\text{Pb}(\text{Zr}_{1-x}\text{Ti}_x)\text{O}_3$ with x close to 50%. Methodologically the prime differences are in the terms that describe the

TABLE I. First-principles parameters for PbZrO_3 in atomic units using the notations of Ref.^{46,47}. The cubic lattice constant in is 7.81362 (a.u.). The normalized ionic displacements derived from Σ_2 mode are $\xi_{\text{Pb}} = -0.445326$, $\xi_{\text{Zr}} = -0.069582$, $\xi_{\text{O}_1} = 0.475535$, $\xi_{\text{O}_2} = 0.748773$, $\xi_{\text{O}_3} = 0.100244$.

AFE on-site	κ_2	0.00049	α	0.00723	γ	-0.00345
AFE intersite	j_1	-0.00392	j_2	0.01190	j_5	-0.00047
	j_3	0.00093	j_4	-0.00007		
	j_6	-0.00011	j_7	0.00015		
Elastic	B_{11}	5.62008	B_{12}	0.80047	B_{44}	0.82796
AFE-strain coupling	B_{1xx}	-0.12962	B_{1yy}	0.14621	B_{4yz}	0.01116
AFE dipole	Z^*	6.3244	ϵ_∞	7.025		
AFD on-site	$\tilde{\kappa}_2$	-0.00059	$\tilde{\alpha}$	0.01721	$\tilde{\gamma}$	-0.01026
AFD intersite	\tilde{j}_1	0.00291	\tilde{j}_2	-0.00028	\tilde{j}_5	0.00056
	\tilde{j}_3	-0.00004	\tilde{j}_4	-0.00276		
	\tilde{j}_6	0.00011	\tilde{j}_7	0.00001		
AFD-strain coupling	$\tilde{B}_{1yyx}, \tilde{B}_{2yyx}$	0.00277	\tilde{B}_{3yyx}	0.02932	\tilde{B}_{4yzx}	0.00113
AFE-AFD coupling	G_{xxxx}	0.00894	G_{xxyy}	0.01926	G_{xyxy}	-0.01396

interactions between the AFD mode and the strain and the AFE and AFD modes.

The total energy of Eq. (1) is used in Metropolis Monte Carlo (MC) simulations to investigate the finite temperature properties of PbZrO_3 . Technically, we simulate the annealing of bulk PbZrO_3 sample modeled by a 16x16x16 supercell with periodic boundary conditions applied along all the three Cartesian directions. The annealing starts at 1500 K and proceeds in steps of 20 K until the temperature reaches 20 K except for the vicinity of the phase transition where the temperature step is reduced to 2 K. For each temperature we used 40,000 MC sweeps. The results from this simulation are shown in Fig. 2. In agreement with some experiments^{37,38}, we find a single transition from a paraelectric cubic phase to an orthorhombic antiferroelectric phase at 946 K. The transition is associated with the condensation of AFD mode in R_4^+ point and AFE mode in Σ_2 point. The AFE vector points along [110] pseudocubic direction while the oxygen octahedra rotate around the AFE vector. Our computational transition temperature overestimates the experimental one of $T_c = 505$ K which could be in part due to the overbinding of structure by LDA

since our Hamiltonian reproduces the zero Kelvin LDA energies precisely. We have also computed the ferroelectric order parameter, however, did not find any ferroelectric phase for the temperatures simulated. To understand the effect of the coupling between the local modes and oxygen octahedron rotations we repeated the annealing simulations with this coupling turned off. In these simulations we still observe condensation of both the AFE and AFD order parameter, however, we find the presence of the following features: i) the transition to the AFE and AFD phases are now decoupled with the latter one occurring at a much higher temperature; ii) both transitions occur at temperatures higher than the computational transition temperature of PbZrO_3 . These suggest that both AFE and AFD are the primary order parameters that compete with each other.

Next we investigate the behavior of PbZrO_3 under an applied electric field. The term that couples local mode to the applied electric field is added to the Hamiltonian of Eq. (1). We carried out two sets of simulations with a *dc* electric field applied along [110] and [111] pseudocubic directions. In these simulations the field is slowly applied, then removed; reapplied in the opposite direction, and then removed again. Such protocol simulates electric field measurements at low frequencies. Fig. 3 shows the field evolution of FE, AFE, AFD and strain order parameters. Panels (a) and (e) give the polarization components as a function of the electric field and demonstrates the double loop structure that is a signature of the AFE behavior. For the field applied along [110] direction the ferroelectric phase is orthorhombic with polarization pointing along [110] direction, while for the field applied along [111] direction the ferroelectric phase is of rhombohedral symmetry with polarization pointing along the [111] direction. Our 300 K saturation polarization of $34 \mu\text{C}/\text{cm}^2$ for the [110] field (and of $28 \mu\text{C}/\text{cm}^2$ for the [111] field) agrees well with the experimentally measured values of $41 \mu\text{C}/\text{cm}^{227}$ and $24 \mu\text{C}/\text{cm}^{228}$. Our computational critical fields are higher than the reported experimental ones^{27,28} owing to the fact that we simulate defect free samples which usually exhibit nearly homogeneous phase transitions. Samples with defects are likely to exhibit inhomogeneous phase transitions that may involve domain formation and propagation that usually lowers switching fields^{22,49}. Therefore, the computational critical fields model the intrinsic critical fields for the material.

Panels (b) and (f) in Fig. 3 show the field evolution of the AFE order parameter. The application of the electric field first results in a small decrease in the magnitude of the order parameter and then a sharp transition into the FE phase. Panels (c) and (g) show the field

evolution of the AFD order parameter. We find that in the AFE phase the AFD order parameter remains parallel to the antipolar axis, while in the ferroelectric phase it prefers to align in parallel to the polar axis. As a result, for the [110] electric field the AFD order parameter does not change its direction throughout the electric field application. Similarly, the direction of the low field AFE order parameter does not change. For the [111] field, on the other hand, the direction of both AFE and AFD order parameters may change as the poling field is removed.

Panels (d) and (h) in Fig. 3 show the electric field evolution for the components of the strain tensor. Here we notice a very large (up to 0.01) change in strain as the structure transitions from the AFE to the FE phase under application of the [111] electric field. For the field along [110] direction the change in strain at the point of the AFE-FE phase transition is rather small. However, the change in the strain due to the FE to AFE transition can reach the values of up to 0.006. Such large strain response to the applied electric field is very attractive for strain and force generators⁵⁰ and electrostrictors⁵¹. We also note the formation of low symmetry monoclinic phases upon application of the electric field.

Next we investigate how the response to the electric field changes with the temperature. Fig. 4(a) shows the hysteresis loops computed at different temperatures. We notice that as the transition temperature approaches the loop area shrinks and the critical field decreases. The temperature dependence of the intrinsic critical field is given in Fig. 4(b). The critical field decreases linearly with the temperature similar to the coercive field in ferroelectrics⁵². The decrease in the critical field was observed experimentally in the vicinity of the phase transition²². The critical fields associated with the electric field applied along the [111] direction are slightly lower than the critical fields that correspond to the electric field applied along the [110] direction. The fact that the intrinsic critical field never crosses the temperature axis suggests that the AFE remains energetically more favorable in the entire temperature range. However, the situation may change in the presence of defects that lower the critical fields and make the FE energetically more competitive. Indeed, Ref.[33] suggests that the FE phase occur in response to the change in calcium concentration. Fig. 4(c) shows the temperature dependence of strain and saturation polarization. Saturation polarization remains nearly constant while there is an anomalous decrease in strain. Similar behavior was also reported for the $(\text{Pb}_{0.97}\text{La}_{0.02})(\text{Sn,Ti,Zr})\text{O}_3$ alloy⁵³.

Next we turn to the effect of hydrostatic pressure on the properties of PbZrO_3 that has

recently received some attention²⁰. Here we apply a hydrostatic pressure in the range of -4 GPa to 4 GPa to study its effect on the PbZrO_3 order parameters at finite temperature. To the best of our knowledge, the finite temperature response of PbZrO_3 to the hydrostatic pressure is currently unknown. Fig. 5(a) shows the pressure dependence of AFE and AFD order parameter at 300 K. We find that the hydrostatic compression favours AFD order parameter and disfavours the AFE one, while the hydrostatic expansion causes the opposite effect. AFD distortions respond to the hydrostatic pressure more strongly as compared to the antipolar ones. The effect of the hydrostatic pressure on the transition temperature is quantified in Fig. 5(b). In agreement with the experimental studies [] we find that the hydrostatic compression results in an increase in the transition temperature. The hydrostatic expansion causes the transition temperature to drop. We attribute this trend to the stabilizing effect that the hydrostatic compression has on the AFD motion.

In summary we have developed a computational model to study antiferroelectric PbZrO_3 from first principles. Application of the model to investigate finite temperature properties of this prototype antiferroelectric demonstrated the existence of a strong coupling between the oxygen octahedron rotation and AFE order parameter for a very large range of temperatures and under applied electric field. The temperature evolution of the double hysteresis loops indicated that the area of the loops shrink as the transition temperature approaches. The intrinsic critical field that induces the AFE-FE phase transition decreases linearly with temperature similar to the coercive field in ferroelectrics. The hydrostatic compression was found to favour the AFD motions and disfavor the AFE distortions that lead to the increase in the transition temperature.

Acknowledgments: The present work is supported by the U.S. Department of Energy, Office of Basic Energy Sciences, Division of Materials Sciences and Engineering under grant DE-SC0005245. This research used resources of the National Energy Research Scientific Computing Center, which is supported by the Office of Science of the U.S. Department of Energy under Contract No. DE-AC02-05CH11231.

-
- ¹ K. M. Rabe, “Antiferroelectricity in oxides: A reexamination,” in *Functional Metal Oxides* (Wiley-VCH Verlag GmbH and Co. KGaA, 2013) p. 221.
- ² A. R. Chaudhuri, M. Arredondo, A. Hahnel, A. Morelli, M. Becker, M. Alexe, and I. Vrejoiu, *Phys. Rev. B* **84**, 054112 (2011).
- ³ B. Jaffe, W. R. Cook, and H. Jaffe, Academic Press, 174 (1971).
- ⁴ K. Yamakawa, K. W. Gachigi, S. Trolier-McKinstry, and J. P. Dougherty, *J. Mater. Sci* **32**, 5169 (1997).
- ⁵ B. Xu, N. G. Pai, and L. E. Cross, *Mater. Lett.* **34**, 157 (1998).
- ⁶ B. Xu, Y. Ye, and L. E. Cross, *J. Appl. Phys* **87**, 2507 (2000).
- ⁷ X. Li, J. Zhai, and H. Chen, *J. Appl. Phys* **97**, 024102 (2005).
- ⁸ O. Yoshiro, United States Patent (1976).
- ⁹ W. Zhong, D. Vanderbilt, and K. M. Rabe, *Phys. Rev. Lett.* **73**, 1861 (1994).
- ¹⁰ L. Bellaiche, A. Garcia, and D. Vanderbilt, *Phys. Rev. Lett.* **84**, 5427 (2000).
- ¹¹ I. I. Naumov, L. Bellaiche, and H. Fu, *Nature* **432**, 737 (2004).
- ¹² N. Choudhury, L. Walizer, S. Lisenkov, and L. Bellaiche, *Nature* **470**, 513 (2011).
- ¹³ I. Ponomareva and S. Lisenkov, *Phys. Rev. Lett.* **108**, 167604 (2012).
- ¹⁴ P. Ghosez, E. Cockayne, U. V. Waghmare, and K. M. Rabe, *Phys. Rev. B* **60**, 836 (1999).
- ¹⁵ U. V. Waghmare and R. K. M., *Ferroelectrics* **194**, 135 (1997).
- ¹⁶ K. Leung, E. Cockayne, and A. F. Wright, *Phys. Rev. B* **65**, 214111 (2002).
- ¹⁷ A. K. Tagantsev, K. Vaideeswaran, S. B. Vakhrushev, A. V. Filimonov, R. G. Burkovsky, A. Shaganov, D. Andronikova, A. I. Rudskoy, A. Q. R. Baron, H. Uchiyama, D. Chernyshov, A. Bosak, Z. Ujma, K. Roleder, A. Majchrowski, J.-H. Ko, and N. Setter, *Nat Commun* **4** (2013).
- ¹⁸ J. Hlinka, T. Ostapchuk, E. Buixaderas, C. Kadlec, P. Kuzel, I. Gregora, J. Kroupa, M. Savinov, A. Klic, J. Drahokoupil, I. Etxebarria, and J. Dec, *Phys. Rev. Lett.* **112**, 197601 (2014).
- ¹⁹ J.-H. Ko, M. Górný, A. Majchrowski, K. Roleder, and A. Busmann-Holder, *Phys. Rev. B* **87**, 184110 (2013).
- ²⁰ S. Prosandeev, C. Xu, R. Faye, W. Duan, H. Liu, B. Dkhil, P.-E. Janolin, J. Íñiguez, and L. Bellaiche, *Phys. Rev. B* **89**, 214111 (2014).

- ²¹ J. Íñiguez, M. Stengel, S. Prosandeev, and L. Bellaiche, *Phys. Rev. B* **90**, 220103 (2014).
- ²² G. Shirane, E. Sawaguchi, and Y. Takagi, *Phys. Rev.* **84**, 476 (1951).
- ²³ H. Fujishita and S. Katano, *J. Phys. Soc. Jpn.* **66**, 3484 (1997).
- ²⁴ H. Fujishita, Y. Ishikawa, S. Tanaka, A. Ogawaguchi, and S. Katano, *J. Phys. Soc. Jpn.* **72**, 1426 (2003).
- ²⁵ Z. Ujma and J. Handerek, *phys. stat. sol.* **28**, 489 (1975).
- ²⁶ H. Fujishita and S. Tanaka, *Ferroelectrics* **258**, 37 (2001).
- ²⁷ I. Kim, S. Bae, K. Kim, H. Kim, J. S. Lee, J. Jeong, and K. Yamakawa, *J. Korean Phys. Soc.* **33**, 180 (1998).
- ²⁸ K. Boldyreva, D. Bao, G. Le Rhun, L. Pintilie, M. Alexe, and D. Hesse, *J. Appl. Phys.* **102**, 044111 (2007).
- ²⁹ D. J. Singh, *Phys. Rev. B.* **52**, 12559 (1995).
- ³⁰ R. Kagimura and D. J. Singh, *Phys. Rev. B.* **77**, 104113 (2008).
- ³¹ M. D. Johannes and D. J. Singh, *Phys. Rev. B.* **71**, 212101 (2005).
- ³² J. A. Rodriguez, A. Etxebarria, L. Gonzalez, and A. Maiti, *J. Chem. Phys.* **117**, 2699 (2002).
- ³³ V. J. Tennery, *J. Electrochem. Soc.* **112**, 1117 (1965).
- ³⁴ S. Robert, *Phys. Rev.* **83**, 1078 (1951).
- ³⁵ X. Dai, J. F. Li, and D. Viehland, *Phys. Rev. B* **51**, 2651 (1995).
- ³⁶ K. Roleder, G. E. Kugel, J. Handerek, M. D. Fontana, C. Carabatos, M. Hafin, and A. Kania, *Ferroelectrics* **80**, 161 (1988).
- ³⁷ B. A. Scott and G. Burns, *J. Am. Ceram. Soc.* **55**, 331 (1972).
- ³⁸ O. E. Fesenkoa and V. G. Smotrakova, *Ferroelectrics* **12**, 211 (1976).
- ³⁹ H. T. Stokes, E. H. Kisi, D. M. Hatch, and C. J. Howard, *Acta. Cryst. B* **58**, 934 (2002).
- ⁴⁰ G. Kresse and J. Furthmuller, *Phys. Rev. B.* **54**, 11169 (1996).
- ⁴¹ G. Kresse and D. Joubert, *Phys. Rev. B.* **59**, 1758 (1999).
- ⁴² D. M. Ceperley and B. J. Alder, *Phys. Rev. Lett.* **45**, 566 (1980).
- ⁴³ J. P. Perdew and A. Zunger, *Phys. Rev. B.* **23**, 5048 (1981).
- ⁴⁴ P. E. Blochl, *Phys. Rev. B.* **50**, 17953 (1994).
- ⁴⁵ ISOTROPY Software Suite, iso.byu.edu.
- ⁴⁶ D. Vanderbilt and W. Zhong, *Ferroelectrics* **206**, 181 (1998).
- ⁴⁷ W. Zhong, D. Vanderbilt, and K. M. Rabe, *Phys. Rev. B* **52**, 6301 (1995).

- ⁴⁸ I. A. Kornev, L. Bellaiche, P.-E. Janolin, B. Dkhil, and E. Suard, Phys. Rev. Lett. **97**, 157601 (2006).
- ⁴⁹ K. McCash, A. Srikanth, and I. Ponomareva, Phys. Rev. B **86**, 214108 (2012).
- ⁵⁰ W. Pan, Q. Zhang, A. Bhalla, and L. E. Cross, J. Amer. Cer. Soc. **72**, 1455 (1989).
- ⁵¹ S. T. Zhang, A. B. Kounga, W. Jo, C. Jamin, K. Seifert, T. Granzow, J. Rodel, and D. Damjanovic, Adv. Mat. **21**, 4716 (2009).
- ⁵² S. Ducharme, V. M. Fridkin, A. V. Bune, S. P. Palto, L. M. Blinov, N. N. Petukhova, and S. G. Yudin, Phys. Rev. Lett. **84**, 175 (2000).
- ⁵³ W. Y. Pan, C. Q. Dam, Q. M. Zhang, and L. E. Cross, J. Appl. Phys. **66**, 6014 (1989).
- ⁵⁴ R. W. Whatmore and A. M. Glazer, J. Phys. C **12**, 1505 (1979).
- ⁵⁵ E. Sawaguchi, J. Phys. Soc. Jpn. **7**, 110 (1952).

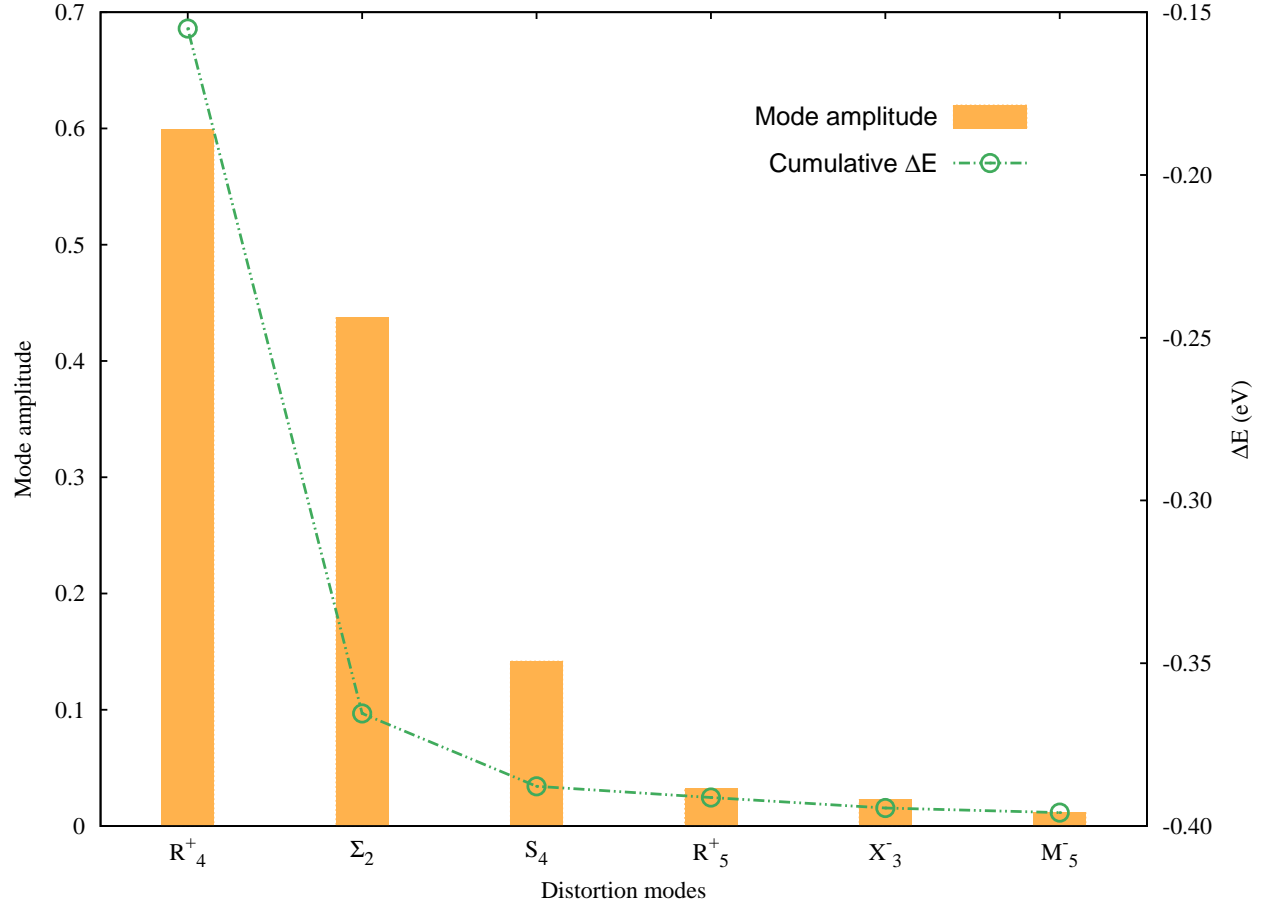


FIG. 1. (Color online). Amplitude of structural distortions of different symmetry in the ground state of PbZrO_3 (shown by rectangles) and the cumulative energy gain (shown by circles) due to addition of each distortion. The energy of undistorted cubic structure is taken as the reference point.

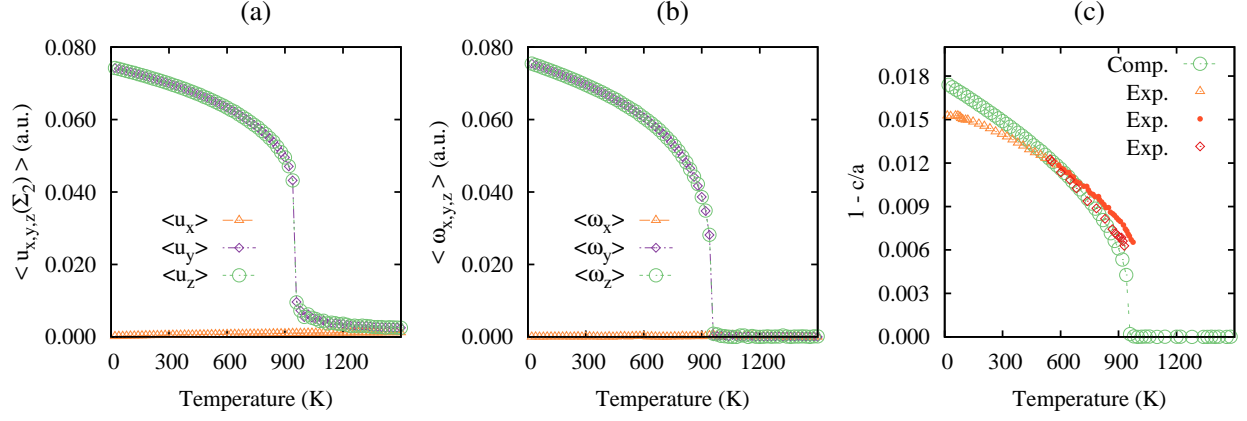


FIG. 2. (Color online). Dependence of the components of the AFE order parameter (a), the AFD order parameter (b), and the lattice distortion $1 - c/a$ (c) on the temperature. Experimental data in panel (c) are from the Refs.^{26,54,55}. They are rescaled to match the experimental and computation transition temperatures.

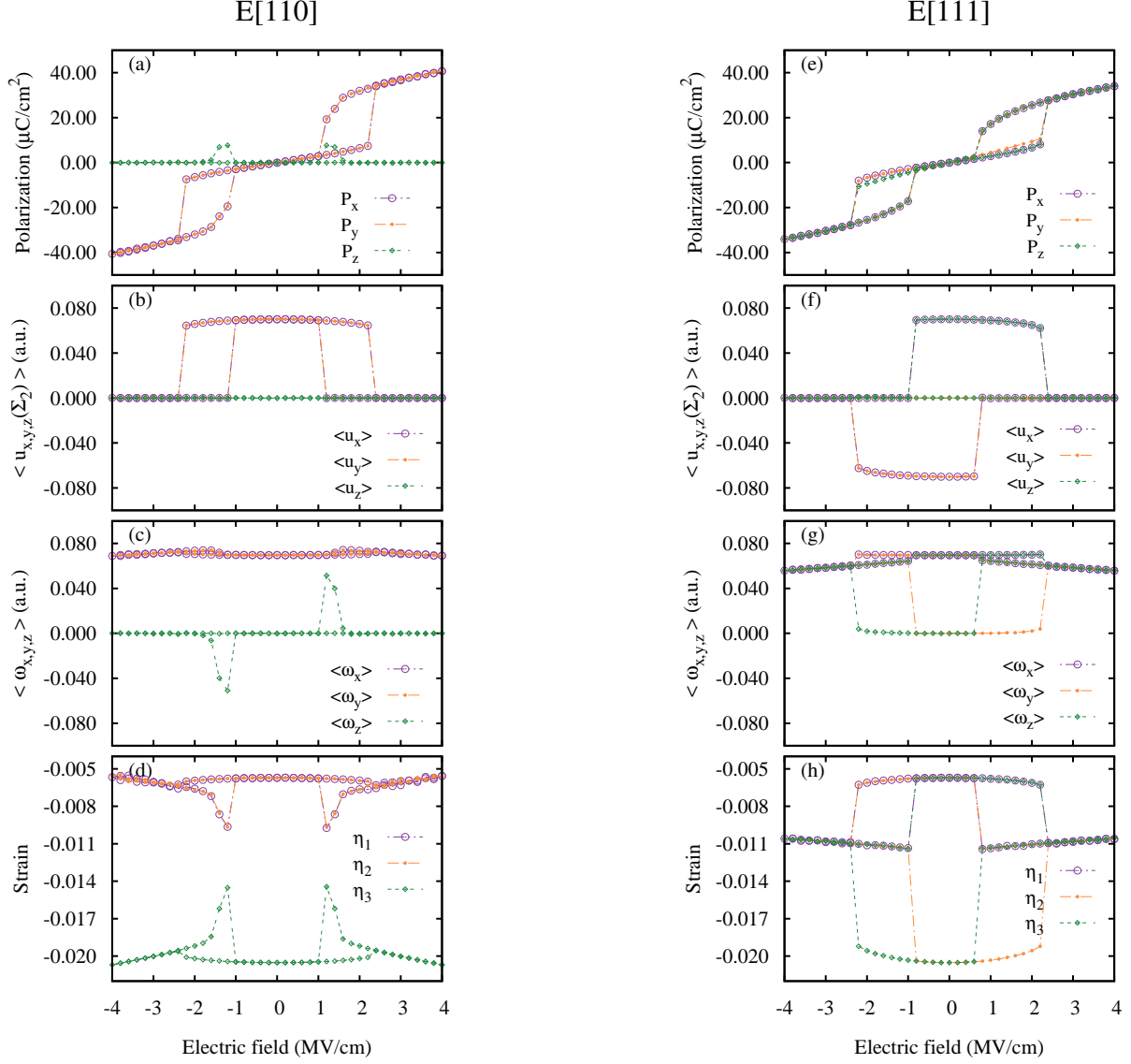


FIG. 3. (Color online). The field evolution of FE, AFE, AFD and strain order parameters: FE order parameter, panels (a) and (e); AFE order parameter, panels (b) and (f); AFD order parameter, panels (c) and (g); strain, panels (d) and (h).

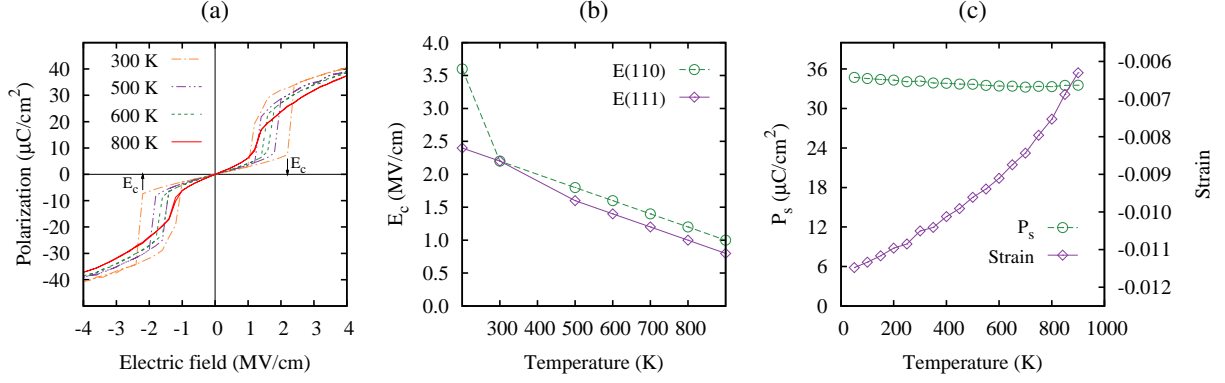


FIG. 4. (Color online) The temperature evolution of the [110] electric-field induced double hysteresis loops (a). Temperature dependence of the critical field (b), and of the saturation polarization and strain (c).

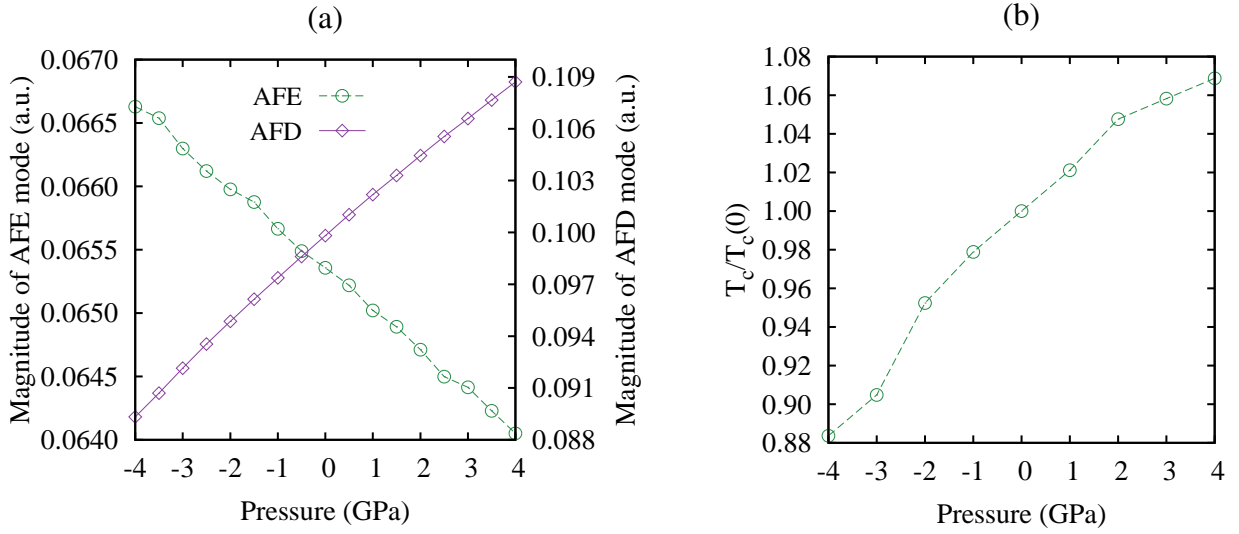


FIG. 5. (Color online). Dependence of the magnitudes of the AFE and AFD modes at 300 K (a) and transition temperature (b) on the hydrostatic pressure. The transition temperatures are normalized by their zero pressure value.